4

Correction of Phase Aberrations in Medical Ultrasound Images Using Signal Redundancy

Yue Li
Information and Communication Technologies Centre
Commonwealth Scientific and Industrial Research Organisation (CSIRO)
Australia

1. Introduction

The pulse-echo technique has been widely used in medical ultrasound imaging. This technique uses an array of transducer elements to transmit a focused beam into the body, and each element then becomes a receiver to collect the echoes. The received echoes from each element are dynamically focused to form an image. Focusing on transmission and reception is performed assuming that the wave propagation speed inside the body is the same everywhere. Unfortunately, the speed inside the body is not constant; it varies from 1470 m/s to greater than 1600 m/s. This speed variation will result in increased side lobes and degraded lateral resolution. Aberration phenomena and their extent in tissue have been evaluated in many works (O'Donnell & Flax 1988; Zhu & Steinberg, 1992; Shmulewitz et al., 1993; Robinson et al., 1994; Hinkelman et al., 1998). The degradation might be tolerable if the frequency is not very high and the aperture size of the array is not very large. However, higher frequencies and larger apertures have been used to improve lateral resolution of ultrasound images. But the resolution improvement cannot be achieved beyond a certain limit, because both larger aperture and higher frequency make the system more sensitive to propagation velocity variations in the body. For example, the four transverse abdominal scan images shown in the first row of Fig.1 were formed with a 64-element linear array using four different aperture sizes (9 mm, 12 mm, 18 mm, and 27 mm) to form each single beam in the image. The array pitch was 1.0 mm and the pulse had a 3.5 MHz centre frequency and 2 MHz bandwidth. The Superior-Mesenteric-Artery (SMA) and the Aorta (A) are the main objects in these images. Because of the shape of the rectus muscles (speed ~ 1580 m/s) and the fat layers (speed ~ 1450 m/s) at this position, the distortions caused by phase aberration in these images can be easily seen. In the 9-mm aperture image, the superior-mesenteric-artery is almost doubled but the artery wall can still be recognized. When the aperture size becomes larger, the distortion becomes worse.

Phase aberration is one of the most important factors that limit improvement to lateral resolution of ultrasound imaging systems. Successful correction of phase aberrations will make it possible to improve the lateral resolution of images. Phase aberration corrected images using the near-field-signal-redundancy algorithm (Li, 1997) are shown in the second row of Fig.1 and the lateral resolution is improved when the aperture size becomes larger. In this chapter, the near-field-signal-redundancy algorithm is described in details. But first, a review of some related methods developed for phase-aberration correction is given. The

phase aberration problem is not unique to medical ultrasound imaging. It exists in almost all imaging areas, such as atmospheric effects in astronomical imaging (Jennison, 1958; Goodman et al., 1966; Ishiguro, 1974; Muller & Buffington, 1974; Buffington et al., 1977; Hamaker et al., 1977; Hogg, 1981; Tyson, 2010), antenna-position errors in radar and microwave imaging (Steinberg, 1991) and weathered-layer-effect in seismic imaging (Yilmaz & Doherty, 1987).

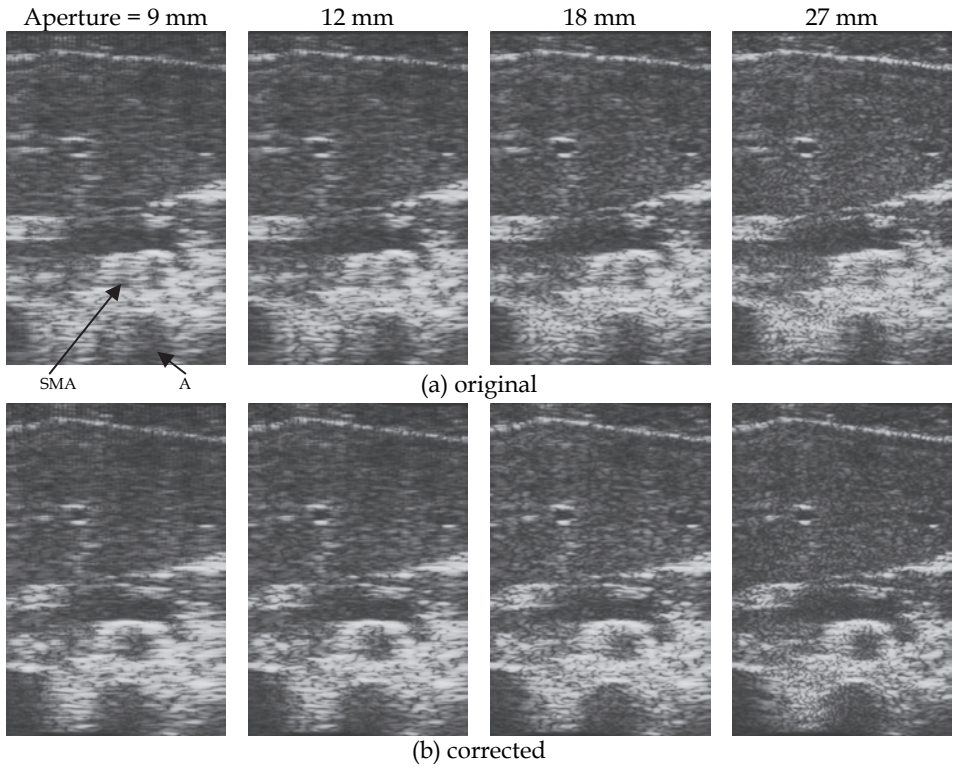

Fig. 1. The resolution of images is only improved with increased aperture size after phase-aberration correction. (a) without phase-aberration correction. (b) with phase-aberration correction.

In astronomical imaging, phase and amplitude aberrations caused by the atmosphere make it difficult to achieve diffraction-limited resolution on the ground. One widely used aberration-correction method is the direct-wave-front-measurement method. This is used when there is a dominant bright star either present or artificially created using laser (Tyson, 2010). A plane wavefront at the aperture should be observed since the dominant point target is in the far field of the imaging aperture. Any departure from a plane wavefront is caused by phase aberration. After measuring the wavefront, the next step is to separate the phase-aberration profile across the aperture from the non-aberrated wavefront. This is not a simple task because the angle of the star is generally unknown. Fortunately, for a target in the far field, such separation is unnecessary since the error of the assumed angle of the star causes a

shift of the image position only and has no effect on focusing. Methods using signals received from arbitrary target distributions have also been developed in astronomical imaging. These include maximum-sharpness (Muller & Buffington, 1974; Buffington et al., 1977) and redundant-spacing interferometer methods. (Jennison, 1958; Ishiguro, 1974) Hamaker et al. (Hamaker et al., 1977) pointed out that these methods are all based on the same fundamental principle: signal redundancy. When the target distribution is complex, there is no prior knowledge about the wavefront shape without phase aberrations. Therefore, the aberration profile cannot be separated directly from the unaberrated wavefront in the measured wavefront. In this case, the signal-redundancy principle makes the separation unnecessary. The redundant-spacing interferometer method does not measure the wavefront but the phase difference between redundant signals, and then directly derives the phase-aberration profile across the array. The result also contains an arbitrary steering angle which has no effect on focusing. The maximum-sharpness method uses a trial-and-error method to adjust each antenna's phase. When an indicator is maximized, the system is in focus. This method is also based on the signal-redundancy principle. When the system is in focus, redundant signals are added in phase and the indicators will be maximized.

Phase-aberration correction methods have also been developed for active (pulse-echo) and near-field imaging systems, such as radar, microwave, ultrasonic and seismic imaging systems. Since the number of references is large, they are not listed here and can be found in the references list in (Li, 1997; Li & Robinson, 2008). When there is a dominant point target in the near field, the first step is again to measure the arrival wavefront from the target. Nearest-neighbor-cross-correlation and indicator (maximum sharpness) methods have been used. The next step is to separate the aberration profile from the unaberrated wavefront, which should be spherical. Without knowing the position of the dominant point target, the phase-aberration profile can be obtained only by estimating the target location. The error in the estimated aberration profile because of the wrongly assumed target position will cause de-focusing in the near field case. The image at the dominant point target will still be well focused (at the wrong position) if this inaccurate aberration profile is used to do the correction, since the two errors cancel each other at that position. But, the correction will become increasingly inaccurate away from that point. This correction is therefore only valid in a region around the dominant target. The size of the region depends on the distance from the target to the aperture, the size of the aperture, and the accuracy of the estimated target position. It can be much smaller than the isoplanatic patch, defined as the region where the phase-aberration value is a constant, if the focusing quality is too poor before phase-aberration correction to estimate the dominant point target position with adequate accuracy. Therefore, aberration correction in the near field may have problems even when a dominant point target is available. In some situations, such as forming an image around the dominant target only, estimating the dominant target position accurately is not so important. On the other hand, it is unusual to have a dominant point target in every isoplanatic patch, or even in the entire image, in medical ultrasonic imaging. Techniques have also been developed which use signals from randomly distributed scatterers that generate speckle in an image to measure the wavefront. In the nearest-neighbor-cross-correlation method, a focused beam is transmitted (try to generate an artificial dominant point target) and the phase aberration profile is derived from the cross-correlation measurements between neighboring elements. An iterative method is used to improve the measurement accuracy. The indicator method has also been used in a speckle-generating region. It is an iterative phase-correction

procedure in which the timing of acoustic signals transmitted and received from individual elements is adjusted to optimize the quality indicator. In a lens and mirror astronomical imaging system it is the intensity-sensitive recorder that generates the necessary cross-correlation process between signals coming from different locations on the lens aperture to produce redundant signals. Phases of redundant signals are difficult to directly compare at optical frequencies. A trial-and-error method has to be used with a deformable mirror to focus the image by maximizing an indicator; this is time consuming and it may not converge to the right position. On the other hand, in a very large baseline, radio astronomy imaging system, phases of redundant signals can be compared directly. In ultrasonic imaging, radio-frequency (RF) signals can be acquired and their phases can be compared directly. Therefore, direct phase-difference measurement between redundant signals can be used. A comparison of the nearest-neighbor-cross-correlation algorithm, the indicator method, and the near-field-signal-redundancy algorithm discussed in this chapter can be found in (Li & Gill, 1998). In seismic imaging, a phase-aberration correction (surface-consistent residual static correction) method using signals coming from a specular reflecting plane has been developed to correct the phase aberration caused by weathered layers near the ground surface. The specular reflecting plane is a special kind of target. It is similar to a dominant point target in that every receiver element receives a dominant echo from it. The difference is that the position of the reflecting point is different for different transmitter or receiver positions. The non-aberrated arrival wavefront from a specular reflecting plane depends on the angle of the plane and the propagation speed between the plane and the array. Common receiver, common transmitter, and common midpoint signals can be used for the measurement. Common midpoint signals are generally preferred because of several advantages, such as insensitivity to the angle of the reflecting plane. It should be noted that common midpoint signals are not redundant when there is a specular reflecting plane in the near field, because the position of the reflecting point is different for different transmitter or receiver positions. Therefore, the seismic method is not a signal-redundancy method.

A least-mean-squares error-fitting method has been developed in ultrasonic imaging (Hirama & Sato, 1984) to form an image of targets on a plane parallel to the transducer array surface through an inhomogeneous layer. The method uses the complete signal set to build an over-determined equation group which has sufficient equations to estimate the spatial frequency components of the target plane and the aberration profiles across the array. The technique requires the area of the target to be small; when the system is in the Fresnel zone, only an approximated image can be obtained. The method will not apply to targets that extend in range. A least-mean-squares error-fitting method using the far-field signal-redundancy principle to measure the phase aberration profile directly has also been developed (Rachlin, 1990). In this method, first, common midpoint signals are cross correlated directly (without compensating for the near field effect, as shown in (11) in Rachlin, 1990) to find the relative time-shift between them, then an over-determined matrix is used to derive the phase-aberration value for each element. When there is no phase aberration, the relative time-shift between common midpoint signals is zero according to (9) and (10) in (Rachlin, 1990), which is true only in the far field. Therefore, this technique is a far-field signal redundancy technique. The analysis in this chapter shows that for targets in the near field, there is a near-field term in the relative time-shift between common midpoint signals. A dynamic near-field-delay correction is proposed to reduce its effect on the measurement. This is the major difference between the near-field signal-redundancy technique described in this chapter and the technique described in (Rachlin, 1990). In

medical ultrasound imaging, dominant point targets, specular reflecting planes, and large areas of uniformly distributed speckle-generating target distributions are unlikely to be found in every isoplanatic patch. The signal redundancy method, which relies very little on target distributions, seems attractive. But, before it can be used in medical ultrasound imaging systems, the near-field effect has to be considered. First, however, the signal redundancy principle for targets in the far field will be reviewed in the next section.

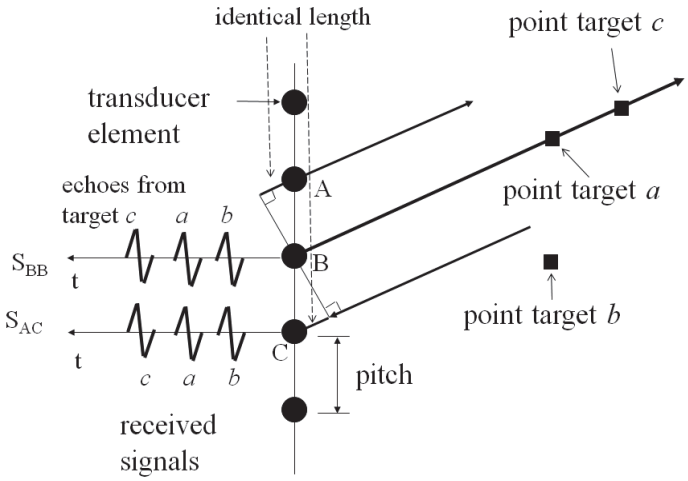

Fig. 2. The signal-redundancy principle for targets in the far field.

2. Signal-redundancy principle in the far field

For an active imaging system, when an array with many small aperture sensors is used to synthesize a larger aperture, it is possible to acquire identical signals using different sensors from arbitrary target distributions in the far field. These signals are termed redundant signals. Common midpoint signals (the middle point position of the transmitter and the receiver is the same) are redundant as shown in Fig. 2. Signal S_{AC} is acquired by transmitting from Element A and receiving at Element C; signal S_{BB} is acquired by transmitting and receiving at Element B. The midpoint of Elements A and C is the center of Element B. Therefore, S_{AC} and S_{BB} are common midpoint signals. When targets are in the far field, *e.g.*, targets *a*, *b* and *c*, S_{AC} and S_{BB} are exactly the same (redundant), because the length of the line segment on the right hand side of Element C and the line segment on the left hand side of Element A in Fig. 2 is the same for targets in all directions. When phase aberrations τ_A, τ_B and τ_C exist at Elements A, B and C, respectively, S_{AC} and S_{BB} will still have the same shape but will have a relative arrival-time difference $2\tau_B-(\tau_A+\tau_C)$, and this information can be used to derive the phase-aberration profile across the array.

These results are valid for short as well as long pulsed signals. They are valid generally for arbitrary target distributions provided that targets are in the far field and the propagation speed is homogenous. The effective aperture concept, defined as the convolution of the transmission aperture *T(z)* and the reception aperture *R(z)* for an active imaging system, is based on the assumption that common midpoint signals are identical; the integration of

$R(z')T(z - z')$ over all z' values adds common midpoint signals (midpoint $z/2$) together with the complex weighting of multiplied sensitivities and added phases of $T(z - z')$ and $R(z')$.

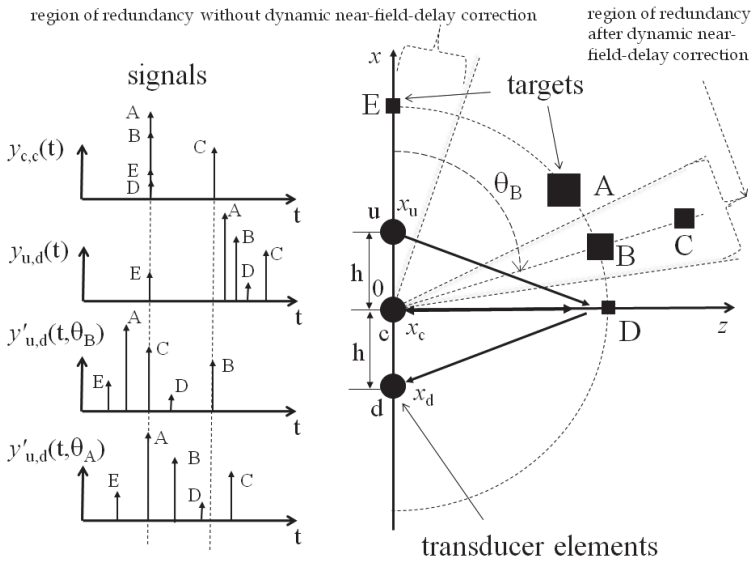

Fig. 3. An active imaging system with targets in the near field and the received and corrected signals when a delta-shaped pulse is transmitted and received.

3. Signal redundancy principle in the near field

For near-field targets, the signal redundancy principle described above is no longer valid. However, although common midpoint signals are not exactly redundant for active near-field imaging, their differences for echoes coming from certain regions can be significantly reduced by a dynamic near-field-delay correction (Li, 1997). Consider a three-element array on the x-axis in Fig. 3**.** The center element c is located at the origin $x = 0$, and the upper element u and lower element d are located at x_u and x_d respectively. It is assumed that $x_u = - x_d = h$. Let $y_{i,j}(t)$ denotes the received signal at element j when element i is the transmitter; $y_{u,d}(t)$, $y_{d,u}(t)$ and $y_{c,c}(t)$ are common midpoint signals; $y_{u,d}(t)$ and $y_{d,u}(t)$ are reciprocal signals, which are identical even for targets in the near field and inhomogeneous media. Assume that transmitted and received signals are delta-shaped pulses. The received signal $y_{c,c}(t)$ is shown in Fig. 3. Echoes coming from targets A, B, D and E arrive at the same time. The received signal $y_{u,d}(t)$ is also shown in Fig. 3. Even though $y_{u,d}(t)$ and $y_{c,c}(t)$ are common midpoint signals, the difference between them is obvious. The echo from target E, which is located on the x-axis, is the only one at the same location in signals $y_{c,c}(t)$ and $y_{u,d}(t)$.

The echo-location difference is larger for targets at angles nearer to the z-axis and at distances closer to the transducer elements. When the distance between the target and the aperture increases, the echo-location difference in $y_{c,c}(t)$ and $y_{u,d}(t)$ decreases, eventually becoming zero at infinite for the far-field situation. The echo-location difference in $y_{c,c}(t)$ and

$y_{u,d}(t)$ reaches its maximum value $2h/c_0$, where c_0 is the wave-propagation speed in the medium, when the target is at the position of Element *c*. A dynamic near-field-delay correction can be used to improve the similarity between $y_{c,c}(t)$ and $y_{u,d}(t)$ for echoes from the region around the *z*-axis of importance for imaging. This correction shifts signals so that envelope peaks of echoes coming from targets in a particular direction line up in the two common midpoint signals. It is the same as the delay process in the "delay-and-sum" dynamic focus image forming algorithm. The signal $y'_{u,d}(t, \theta_B)$, which is the corrected version of $y_{u,d}(t)$, with the correction angle in the direction of targets B and C is shown in Fig. 3. The positions of echoes coming from targets B and C in $y'_{u,d}(t, \theta_B)$ are the same as those in $y_{c,c}(t)$. That is, for echoes coming from these two targets, $y'_{u,d}(t, \theta_B)$ and $y_{c,c}(t)$ are redundant. But the positions of echoes from targets A, D and E in $y'_{u,d}(t, \theta_B)$ are different from that in $y_{c,c}(t)$, since these targets are not at the correction angle. The corrected signal $y'_{u,d}(t, \theta_A)$ at angle of target A is also shown in Fig. 3.

A pulse with non-zero length will cause problems even for echoes coming from targets at the correction angle. For example, to make the echo from target B identical in $y_{c,c}(t)$ and $y_{u,d}(t)$, the whole pulse has to be moved with the same correction as that for the peak of the pulse envelope. But, since these echoes are overlapping, it is impossible to separate pulses from different depths (and angles) and move them separately. One can only do a dynamic delay correction as for a delta-shaped pulse. This will stretch the echo since the leading part of an echo is always shifted forwards more than its trailing part. Therefore, for a pulse of finite length, the dynamically corrected common midpoint signals are not strictly identical even for echoes coming from targets at the correction angle; the longer the pulse, the larger the difference. Fig. 5 in (Li. 1997) compares echoes coming from targets A, B, and D separately in $y'_{u,d}(t, \theta_B)$ and $y_{c,c}(t)$. The echo from target B in $y'_{u,d}(t, \theta_B)$ is stretched compared to that in $y_{c,c}(t)$ but their envelope peaks are coincident (Fig. 5(b)). The echo from target A in $y'_{u,d}(t, \theta_B)$ is stretched compared with that in $y_{c,c}(t)$, and its envelope peak is shifted forward because of overcorrection. The echo from target D in $y'_{u,d}(t, \theta_B)$ is stretched and shifted backward because of undercorrection.

After a dynamic near-field-delay correction, common midpoint signals will not become exactly redundant in the near field. But, they will be more similar for echoes coming from the region of interest. Within a specified error, the echoes coming from the region of interest can be regarded as redundant. The question is, given a pulse length L and an acceptable phase error limit ϕ_0, in what angular range should targets be for their echoes to become redundant in common midpoint signals after a dynamic near-field-delay correction? This question has been answered in (Li, 1997). Before the dynamic near-field-delay correction, the region of redundancy is around the *x*-axis (Fig. 3), which is not a region of interest. After the dynamic near-field-delay correction, the region of redundancy is around the correction angle. If transducer elements have some degree of directivity, so that their angular response is limited to the region of redundancy around the correction angle, the dynamic near-field-delay correction can increase the similarity between common midpoint signals in the near field. It has been shown in (Li, 1997) that common-midpoint signals are still a special group of signals in the near field because, after the dynamic near-field-delay correction, they are much more similar to one another compared with corrected signals in other signal groups. This is termed the near-field signal-redundancy principle.

For linear arrays, the element size is usually considerably larger than the wavelength. Therefore the beam width of each element is small and most signal energy is from the region of redundancy when the correction angle is around 90°. As a result, common-midpoint signals can be considered as redundant after the dynamic near-field-delay correction.

For phased arrays, the element size is usually smaller than a wave length and the beam of each element is wide. This causes two major problems. One problem is that the similarity between common-midpoint signals is not improved by the dynamic near-field-delay correction. It only shifts the region of redundancy to the area around the correction angle. Another problem is that echoes coming from different angles may experience different aberration values, which makes it impossible to measure the phase aberration profiles using the linear array algorithm. The sub-array method proposed in (Li, 2000a, 2000b; Li & Robinson, 2000b) can be used to solve both problems, if the phase-aberration value for elements in the same sub-array can be considered as the same in all directions. This requirement may limit the maximum size of sub-arrays, and therefore limit the narrowest achievable beamwidth and the maximum spatial frequency of the aberrator that can be successfully measured. In this method, sub-arrays are formed of adjacent groups of elements to narrow the beams used to acquire common-midpoint signals and steer the beam direction, so that the similarity between common-midpoint signals is increased and angle-dependent, phase-aberration profiles can be measured. There are several methods can be used to implement the dynamic near-field-delay correction on common-midpoint signals collected with sub-arrays. These methods have different computation loads and the degree of similarity between common-midpoint signals collected in these methods is also different. The performance of these methods has been analyzed and compared theoretically in (Li, 2000b).

For two-dimensional arrays, besides using elements along a straight line, there is another element configuration that can be used to acquired common-midpoint signals, which does not exist for one-dimensional arrays. Consider four adjacent, point-like transducer elements (Fig. 4) in a two-dimensional array. They are labeled as Element 1, 2, 3 and 4 and located in the x-y plane at ($p_x/2$, $p_y/2$), ($-p_x/2$, $p_y/2$), ($-p_x/2$, $-p_y/2$) and ($p_x/2$, $-p_y/2$), respectively, where p_x and p_y are array pitches in the x and y directions respectively. $y_{2,4}(t)$ and $y_{1,3}(t)$ are common midpoint signals, because the midpoints between their transmitters and receivers are located at the same point (the origin in Fig. 4). It has been shown (Li & Robinson, 2008) that without the dynamic near-field-delay correction, the region of redundancy is between two rectangular hyperbolas (Fig. 5), which is in the direction of interest for imaging. This is different from the case of one-dimensional arrays, where, without the dynamic near-field-delay correction, the region of redundancy is in the direction of the axis that goes through the three consecutive transducer elements used to acquire common-midpoint signals (Fig. 3), which is not in the direction of

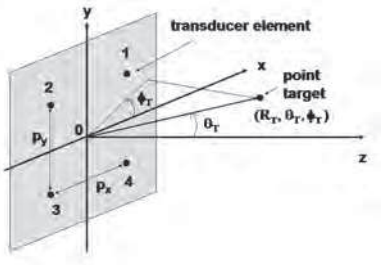

Fig. 4. A four-element sub-aperture in a two-dimensional array.

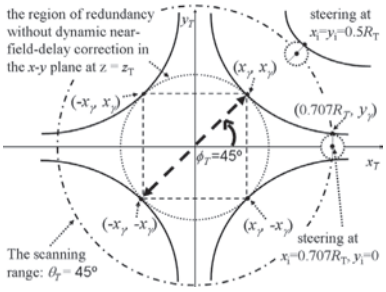

Fig. 5. The region of redundancy (not to scale).

interest for imaging. The region of redundancy is narrowest in the direction of $\phi_T = \pm 45^o$ (Fig. 5). The region of redundancy can be approximately defined as inside the circle within those hyperbolas as shown in Fig. 5. Many properties of the region of redundancy have been theoretically derived in (Li & Robinson, 2008).

As in the case of one-dimensional arrays, the region of redundancy for common-midpoint signals acquired with four adjacent transducer elements can also be shifted to other directions with the dynamic near-field-delay correction. This is a useful property for measuring angle-dependent phase-aberration profiles using sub-arrays and it has been theoretically analyzed in (Li & Robinson, 2008).

In this section, the near-field signal redundancy principles have been discussed for linear, phased and two-dimensional arrays. In the next section, phase-aberration correction algorithms based on these principles are introduced and experimental results are presented.

4. Aberration correction using near field signal redundancy

4.1 Algorithm for linear arrays

Since the array pitch of linear arrays are much larger than the center-frequency wave length of the transmitted pulse, each element has a relatively narrow beam in the z-axis direction. However, the beam cannot be steered. A sub-aperture of the array is used to form an image line and the whole image is formed by sliding the sub-aperture across the array. The linear array algorithm for phase-aberration correction based on the near-field signal-redundancy principle was proposed in (Li, 1997). A few important considerations relating to this algorithm are discussed here.

For each midpoint position, many common midpoint signals can be acquired using a linear array. However, only the closest common midpoint signal pairs (acquired using three adjacent elements) should be used because the near-field effect is smallest for these signals. The received signals are dynamically corrected at the 90^o angle. The normalized cross-correlation functions are calculated at a selected depth with a selected window length. The region chosen for correlation should be the region in which one wants to improve the lateral resolution. The length of the correlation window should be chosen so that the signal experiences the same aberration effect, *i.e.* in the same isoplanatic patch. On the other hand, it should be as long as possible to improve the signal-to-noise ratio of cross-correlation functions. The dynamic near-field-delay correction can also be applied at a few angles and the peak position of the cross-correlation function with the maximum cross-correlation coefficient is chosen for deriving the phase-aberration profile.

For an N element array, there are N-2 pairs of common-midpoint signals and measured peak positions. They are related to the phase error at each element by equation (26) in (Li, 1997). The phase aberration profile can be derived assuming that the phase-aberration values for the two elements at the ends of the array are zero. This assumption causes a linear-component error (the ambiguity profile) between the derived phase-aberration profile and the real phase-aberration profile. If the ambiguity profile is small, its effect is approximately a global rotation and range shift of the image. If it is large, it will influence the focusing quality. A detailed analysis of the influence of ambiguity profiles on focusing in the very near field can be found in (Li, 2002a, 2002b).

Errors in peak position measurements of cross-correlation functions will be magnified in the process of deriving the phase aberration profile. Results of theoretical analysis in (Li, 2007) indicate that the accuracy requirement on the peak position measurement is very high for an

array with a large number of elements. For a 64-element array, the bias in the peak-position measurement is magnified by a factor up to 496. Assume that the acceptable largest bias of the derived phase-aberration value is one radian, then the measurement bias needs to be less than 1/496 radians, which is a very strict requirement. Assuming that a constant or linear profile does not influence focusing, the requirement is relaxed to 1/325 radians, and the maximum bias value in the derived phase aberration profile occurs at the ends of the array. The standard deviations of peak position measurements also have to be small in order to measure the phase-aberration profiles accurately. For a 64-element array, the maximum standard deviation in the derived phase-aberration profile is about 72 times the standard deviation of the measured peak position; the *rms* is 52 times, or 25 times if the constant and linear profiles are considered as harmless.

The strict accuracy requirement on peak position measurements creates a new problem. The timing of electronic channels (receiver and transmitter) has to be calibrated accurately. The requirement for channels to be considered as identical is much stricter for phase-aberration measurement than for image formation. Therefore, the system calibration on a commercial machine usually is not accurate enough. The timing errors of channels are part of the phase aberration profile and they make phase aberration profiles for transmission and reception different. When the timing error difference between transmission and reception channels connected to the same element is small enough for the purpose of image formation, the method proposed in (Li, 1997) can be used to solve this problem. The two reciprocal signals $y_{u,d}(t)$ and $y_{d,u}(t)$ (Fig. 3) are dynamically corrected and cross-correlated with $y_{c,c}(t)$ separately. The two peak positions are then averaged and used to derive the phase aberration profile, which can be used for both transmission and reception phase-aberration corrections. There is no need to measure the transmission and reception phase aberration profiles separately. That is, when the difference between transmission and reception phase-aberration profiles is small for image-formation purpose but large for phase-aberration measurement, they have to be treated as different when performing the phase-aberration measurement, but they can be treated as the same in the image-formation process after the measurement. If the difference is large for imaging purpose, they need to be measured separately. In this case, the reciprocal-signal method proposed in (Li, 2008) can be used.

To perform the dynamic near-field-delay correction, the array pitch and the average propagation speed in the medium need to be known. How accurately these parameters need to be known for the near-field signal-redundancy algorithm to perform properly? This has been analyzed in (Li et al., 1996). If the array pitch and propagation speed are not known accurately, the formed image (image formation also uses the two parameters) will also be distorted even if the medium is homogeneous. That is, phase aberrations are introduced by incorrect pitch and speed values and the phase aberration profile across the array is different at different points in the image. It has been shown in (Li et al., 1996) that the near-field signal-redundancy algorithm is capable of correcting phase aberrations generated by pitch and speed errors. Therefore, the array pitch and average propagation speed need not to be known very accurately. However, large errors will reduce the size of the isoplanatic patch and therefore require more phase-aberration profiles to be measured to correct the whole image (Li et al., 1996).

The near-field signal-redundancy algorithm for linear arrays typically includes the following steps:

1. Common midpoint signals are acquired.
2. Dynamic near-field-delay corrections are applied at a proper angle.

3. The dynamically corrected common midpoint signals are cross-correlated at a selected depth with a selected window length.
4. The relative time-shift between common midpoint signals are measured from the peak position of the cross-correlation functions.
5. The relative time-shifts between $y_{u,d}(t)$ and $y_{c,c}(t)$ and between $y_{d,u}(t)$ and $y_{c,c}(t)$ are averaged.
6. The phase-aberration profile across the array is derived.
7. If necessary, the undetermined linear term (ambiguity profile) is adjusted to optimize the performance of the system.

This algorithm has been experimentally tested (Li et al., 1997). The system used to test this algorithm was based on a Toshiba model SAL-32B 8-channel Scanner. This system has 64 transmission channels, 8 reception channels multiplexed across the array. This system is capable of separately transmitting on each individual element, and receiving on eight channels at a time. It can be switched between the normal real-time scan mode and the single-element-transmit/multiple-element-receive data collecting mode. A 64-element linear array was used with a pitch of 1.0 mm and an element width of about 1.0 mm. The element height is 10 mm, and the focus of the lens in the elevation direction is at about 60 mm. The received pulse has a 3.5 MHz centre frequency and 2 MHz bandwidth.

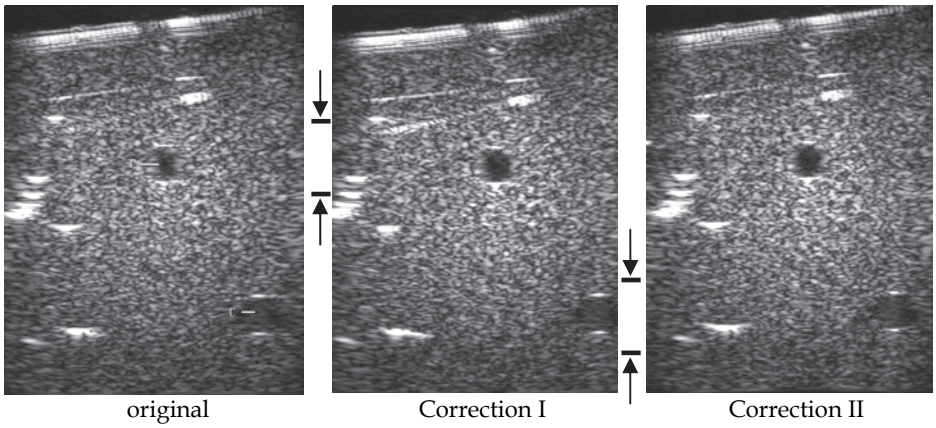

Fig. 6. Correction results of images from a tissue mimicking phantom with an aberrator.

4.1.1 Experimental results from a tissue-mimicking phantom

The data were acquired from a tissue-mimicking phantom overlaid by an aberrator. The aberrator has a speed of 1420 ms^{-1} and an attenuation coefficient 1.2 dB $cm^{-1}MHz^{-1}$. The shape of the aberrator is shown in Fig. 1 in (Li et al., 1997). Two aberrating structures were cut out and put above the two cysts in the phantom. The speed of the aberrator is close to that of fat. Since the array is one-dimensional, the structure of the aberrator is also one-dimensional. The tissue mimicking phantom was RMI-413, but is an earlier version and the cysts are 6 mm, not 7.5 mm, in diameter.

The original aberrated image and two corrected images are shown in Fig. 6. The first correction used signals coming from a depth near the upper cyst (indicated by arrows). The second correction used signals from a depth near the lower cyst. The two cysts are distorted

in the original image, and the distortions in the original image are partially corrected in the two corrected images.
For comparison, the results from the same phantom without the aberrator are shown in Fig. 7. The difference between the original and corrected is very small because the measured phase-aberration profile has very small values (Li et al., 1997), which indicates that the noise level and other parameters were reasonable for the successful measurement of phase-aberration profiles.

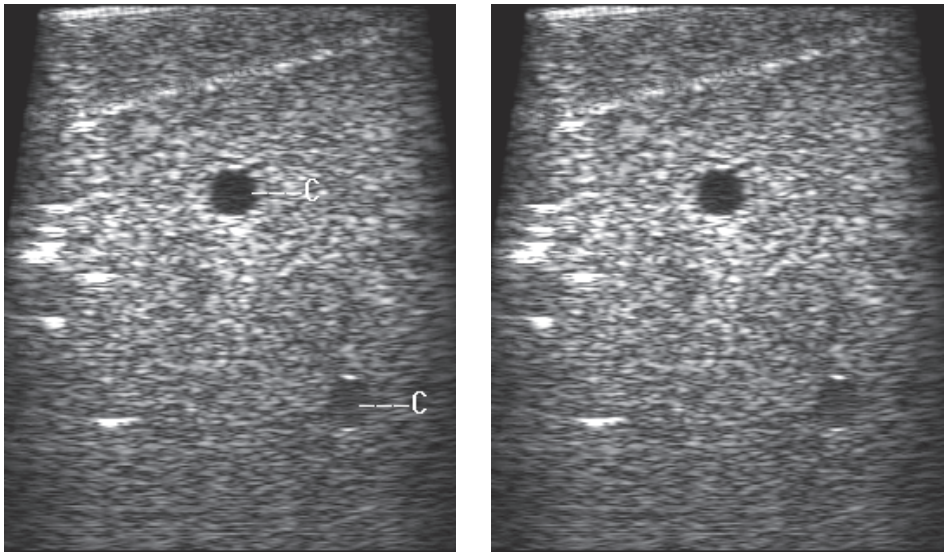

original corrected

Fig. 7. Correction results of images from a tissue mimicking phantom without the aberrator.

4.1.2 Experimental results from volunteers

Data were acquired from a group of volunteer subjects. Since the height of elements in the linear array was large (10 mm) and the algorithm requires that phase aberration values for echoes received at an element can be considered as the same, transverse abdomen scan was used because of the structure of muscles and fat layers in that position. The system was operated in the normal real-time scanning mode to scan for an aberrated image, and then switched to the synthetic-aperture mode to acquire data.
Fig. 8 shows the original and two corrected images from Volunteer 1. The superior-mesenteric-artery (SMA) and the aorta are used as the main objects to evaluate the quality of the images. In the original image the SMA and the aorta are distorted. In the corrected images, their boundaries are much better defined and their shape is more circular. Fig. 9 shows the results from Volunteer 2. The boundaries of the SMA and the aorta are better defined in the corrected image than they are in the original image. Fig. 10 shows the results from Volunteer 3 using data from three different depths. The boundaries of the SMA and the aorta are better defined in the corrected images; the Splenic Vein (SV) is also much clearer in the corrected image. This data set is the same as that used to form images in Fig. 1.

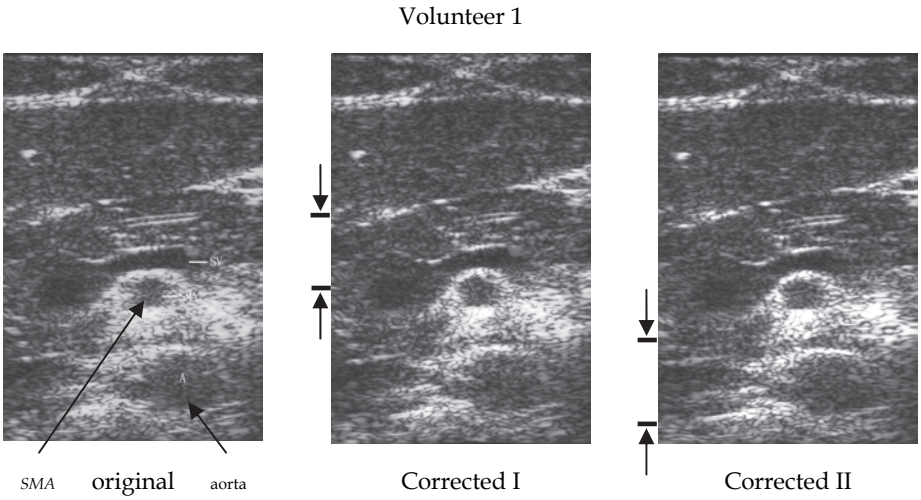

Fig. 8. Correction results of images from Volunteer 1.

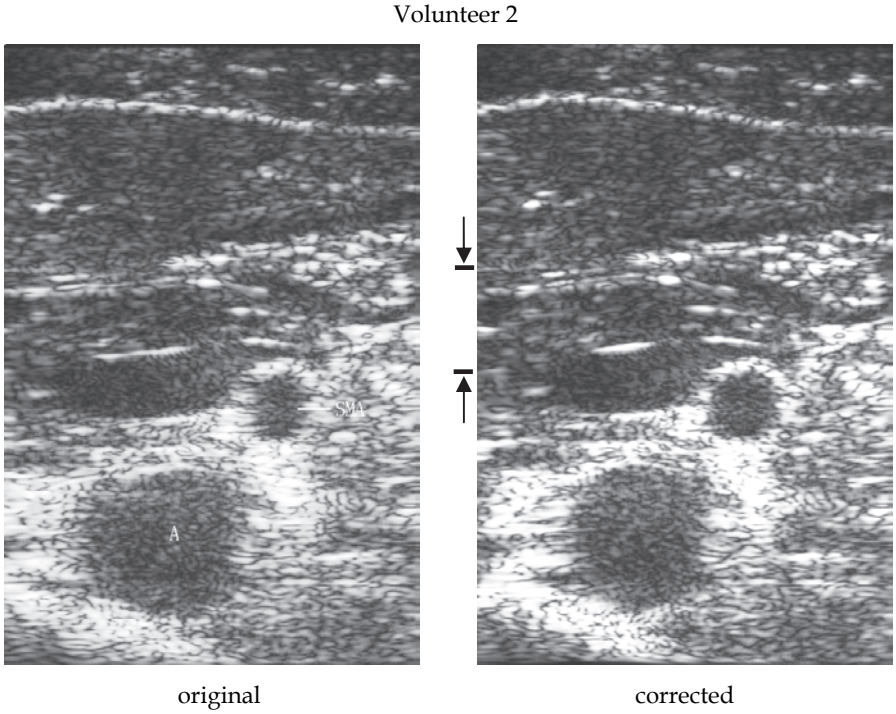

Fig. 9. Correction results of images from Volunteer 2.

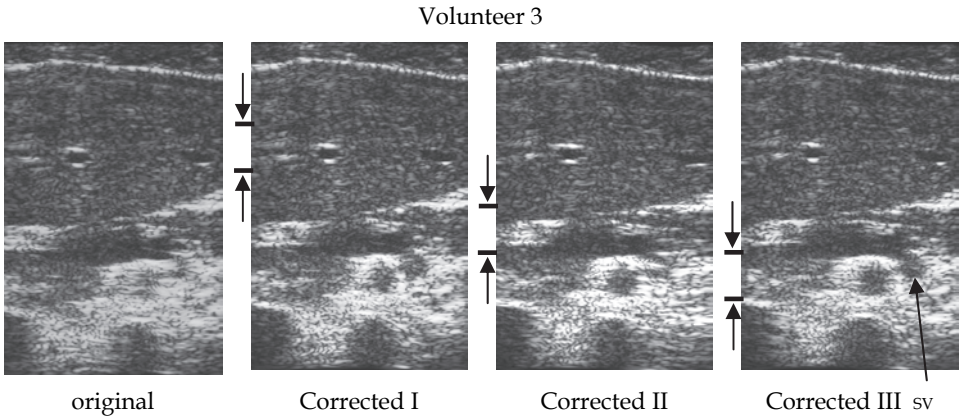

Fig. 10. Correction results of images from Volunteer 3.

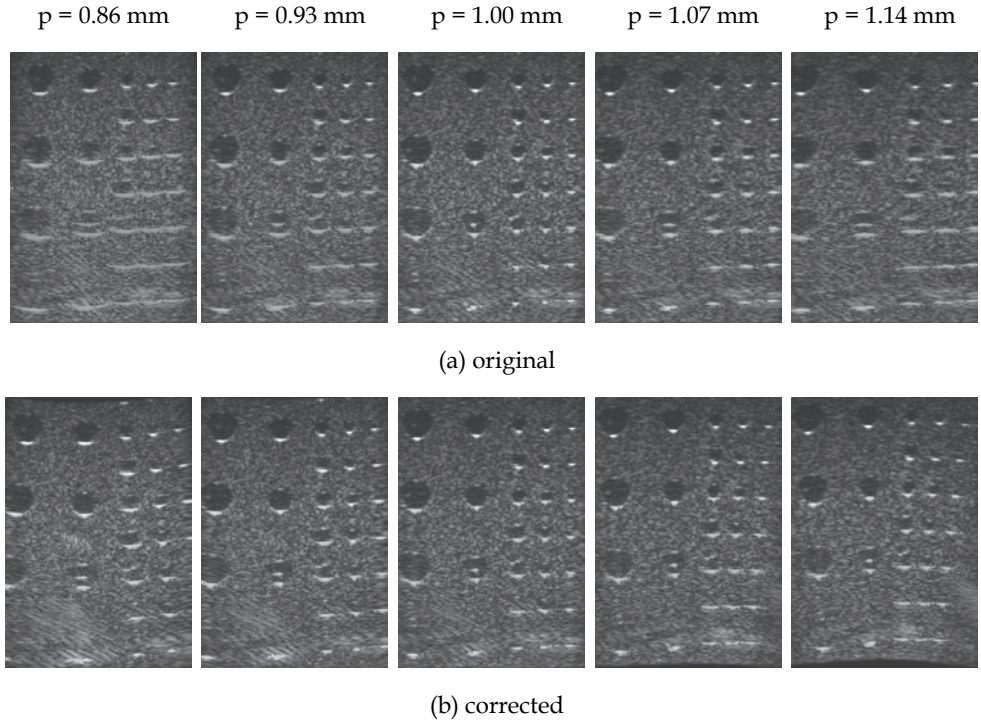

Fig. 11. Results of correcting phase aberrations generated by incorrect pitch values.

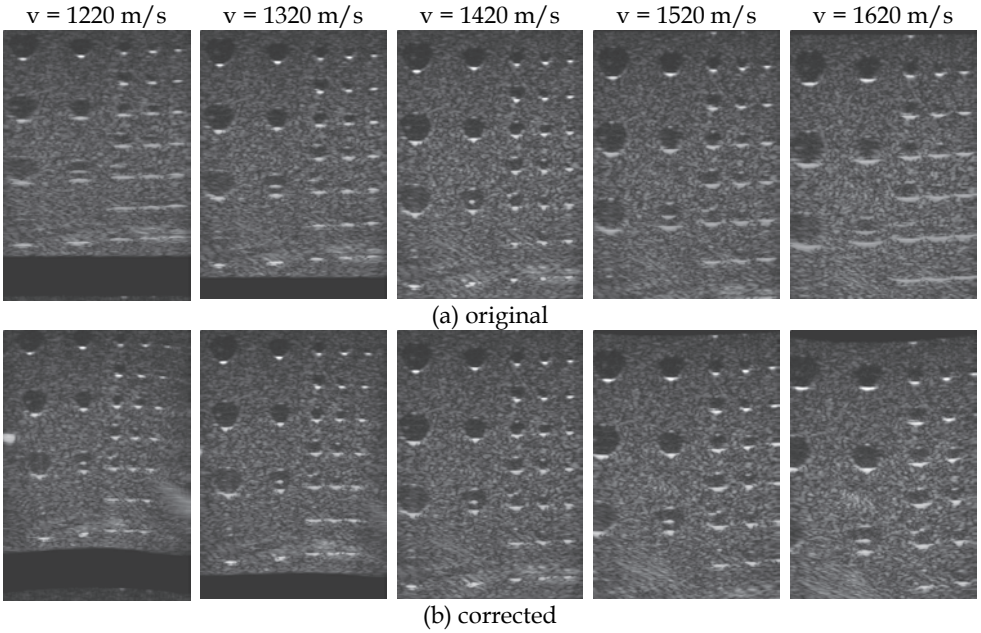

Fig. 12. Results of correcting phase aberrations generated by incorrect speed values.

4.1.3 Experimental results of correcting phase aberrations generated by incorrect pitch and speed values

Data acquired from a tissue-mimicking phantom without any aberrator were used to test the performance of the linear array algorithm on correcting phase aberrations generated by incorrect array pitch and propagation speed values. The phantom had a propagation speed of 1420 m/s. The true array pitch was 1.00 mm. The synthetic aperture image formed using five pitch values and five speed values are shown in Figs. 11(a) and 12(a), respectively, and the image in the middle was formed with the correct value. The size of the images is 45 mm x 55 mm. Images formed with incorrect values are significantly distorted. Phase aberration profiles were measured using the linear array algorithm with the incorrect pitch and speed values. The signal range used in the measurements was around the fourth row of small cysts. The corrected images are shown in Figs. 11(b) and 12(b), respectively. The correction has restored the focus, especially in the region around the fourth row of small cysts. By measuring several phase aberration profiles using signals from different depths, the whole image can be improved, as it is demonstrated later in the chapter with images formed using phased arrays. These corrected images also show distortions (expansion or compression) in both lateral and axial directions caused by ambiguity profiles (Li et al., 1996).

4.2 Algorithm for phased arrays

The sub-array algorithm for small-element arrays has been proposed in (Li & Robinson, 1997; Li, 2000b). It can be used to overcome problems caused by the wide beam and angle-dependent aberration profiles. This sub-array algorithm typically includes the following steps:

1. Choose a sub-array size. The optimal sub-array size depends on the aberrator properties; therefore, it is difficult to determine in advance. A trial-and-error method may have to be used.
2. Acquire individual signals (transmit at one element and receive at one element) by transmitting at one element at a time and receiving at several elements. The number of receiving elements depends on the size of sub-arrays.
3. Form common-midpoint signals acquired with sub-arrays at several steering directions or imaging lines at selected angle intervals.
4. Calculate the normalized cross-correlation function between these common-midpoint signals at a selected depth with a selected window length.
5. Measure relative time-shift between common-midpoint signals from the peak position of these cross-correlation functions.
6. Derive the phase-aberration profiles across the array for each steering angle or image line.
7. Assign the derived phase-aberration value for each sub-array to each element in that sub-array.

4.2.1 Experimental results from a tissue-mimicking phantom

This algorithm has been successfully tested on data acquired from a tissue mimicking phantom with an aberrator (Li & Robinson, 2000b). The imaging system was a modified ATL Ultramark® 8. The transducer used was an ATL 48-element phased-array with 0.28 mm pitch and 3.0 MHz center frequency. The azimuthal cross-section from the center of the transducer is shown in Fig. 13. The aberrator was made from cast RTV, which had a sound

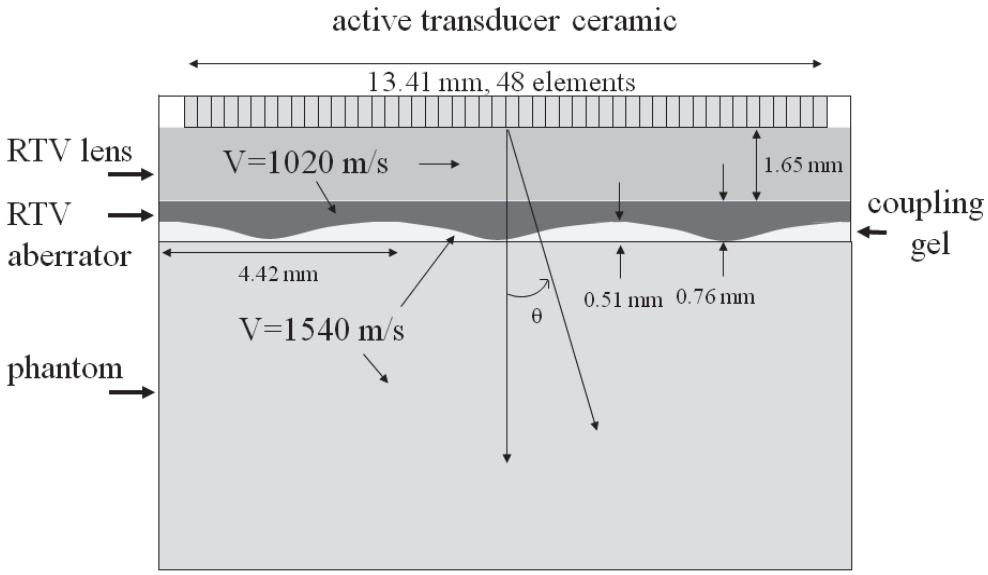

Fig. 13. The azimuthal center cross-section of the ATL transducer with the aberrator attached to its front surface.

velocity of 1020 ms^{-1}, and an attenuation coefficient 1.5 dB mm^{-1} at 3 MHz. The aberrator had a sinusoidal surface, the peak-to-peak range of the sinusoidal wave was 0.51 mm and the period was 4.42 mm. The total active aperture of the array was about 3.03 wavelengths of the sinusoidal wave. The total thickness of the aberrator was about 0.76 mm. The aberrator was cast so that its inner surface conformed to the surface of the elevational focus lens of the array. The potential space between the lens and the aberrator was filled with ultrasound coupling gel, which had a sound speed of 1540 ms^{-1}. Coupling gel also filled the space between the sinusoidal surface of the aberrator and the phantom.

The aberrator introduces a (one-way) phase-error of almost exactly π-radians at 3 MHz. The unaberrated image of the RMI 413 phantom is shown in Fig. 14(a), which was obtained with the same transducer without the aberrator at approximately the same location on the phantom. The image of the phantom from the data set collected with the aberrator attached to the transducer is shown in Fig. 14(b). It is severely aberrated; each point target is tripled with reduced resolution, and the contrast ratio of the anechoic cystic structures is significantly reduced.

To demonstrate the problem related to the wide beam of small elements, we first use the linear-array algorithm to correct the phase aberration. The correction angle for the dynamic near-field-delay correction was at 90° (perpendicular to the array) and the measured profile was used to correct phase aberrations for all image lines (Fig.14(c)). The image quality near the 90° direction has been improved, revealing a column of point targets. The image quality at other directions has not been improved as much. There are no means to measure angle-dependent, phase-aberration profiles without forming sub-arrays. Note that by performing the dynamic near-field-delay correction at different angles in a single-element measurement one does not measure the aberration profiles at different directions. To demonstrate this, phase-aberration profiles were measured with 19 different correction angles, from 45° to 135° at 5° intervals. The measured aberration profiles were very similar for these correction angles (Li & Robinson, 2000b) and the corrected image (Fig. 14(d)) is very similar to that in Fig. 14(c). To measure angle-dependent phase-aberration profiles, sub-arrays need to be formed to narrow and steer the beams. In the sub-array algorithm, each sub-array was formed with three elements (16 sub-arrays in total). The beams of sub-arrays were formed with the synthetic aperture approach and were dynamically focused both on transmission and reception at a correction angle (the beam steering direction). The formed beam had a theoretical -6 dB (two-way) beamwidth of about 20.5° (Li & Robinson, 2000b). It subtended about 0.17 wavelengths of the sinusoidal aberrator. Beams were steered at 19 different angles, from 45° to 135° at 5° intervals, and 19 phase-aberration profiles were derived. The corrected image using the measured phase-aberration profile at the 90° beam steering angle for all images lines is shown in Fig. 15(a) and the focusing quality is only improved around the 90° direction. Similarly, using the phase aberration profile measured at the 105° beam steering angle to correct all images lines only improved the focusing quality around the 105° direction (Fig. 15(b)). The corrected image using all 19 measured profiles is shown in Fig. 15(c) and resolution is improved in all directions. However, the image quality in regions near the left and right boundaries of the image has not improved as much. This is because the strong refraction effect (between RTV and coupling gel) at those angles makes it difficult to measure the aberration profiles accurately in those directions. The aberration values for the two sub-arrays at the two ends of the array are different, and the difference

depends on the steering angle. By assuming that they are zeros in the process of deriving the aberration profile, different ambiguity profiles are introduced in the derived aberration profiles at different steering angles. For targets far from the transducer, where the angle from an image pixel to all elements is approximately the same, the changing ambiguity profile will not influence the focusing of the system at each pixel; however, the image may become distorted (change of target shape). For targets near the transducer, where the angle from an image pixel to each element varies, the focusing quality is reduced at that pixel because of the different ambiguity profiles for the derived aberration profiles from different steering angles. The derived aberration profiles were adjusted by adding a proper ambiguity profile and the corrected image is shown in Fig. 15(d). The image quality is further improved.

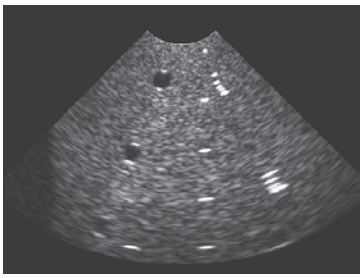

(a) without the aberrator

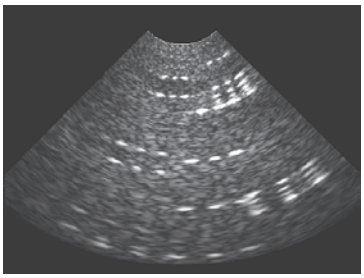

(b) original with the aberrator

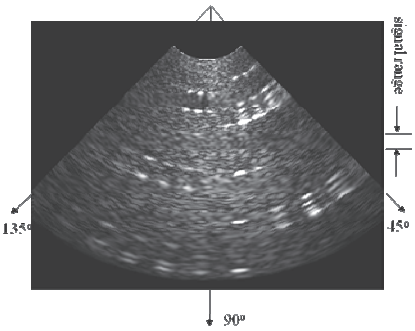

(c) The corrected image using the phase-aberration profile derived without forming sub-arrays at correction angle 90°.

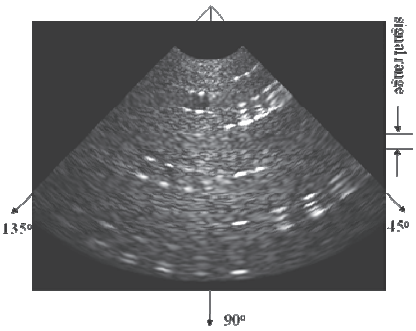

(d) The corrected image using 19 phase-aberration profiles derived without forming sub-arrays and at 19 correction angles between 45° and 135° at 5° intervals.

Fig. 14. (a) Original image without the aberrator. (b) Original image with the aberrator. (c) The corrected image using the phase-aberration profile derived without forming sub-arrays at correction angle 90°. (d) The corrected image using 19 phase-aberration profiles derived without forming sub-arrays and at 19 correction angles between 45° and 135° at 5° intervals.

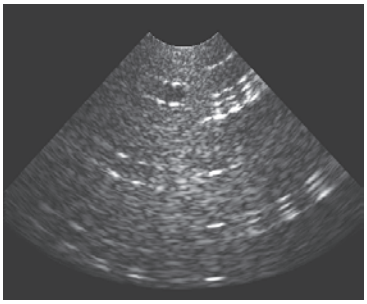

(a) The corrected image using the measured phase-aberration profile at the 90° beam steering angle for all images lines.

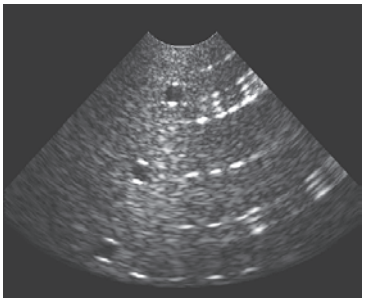

(b) The corrected image using the measured phase-aberration profile at the 105° beam steering angle for all images lines.

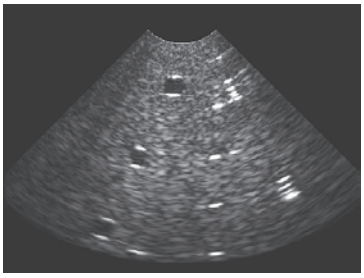

(c) The corrected image using the phase-aberration profile derived with the steering angle-based sub-array method.

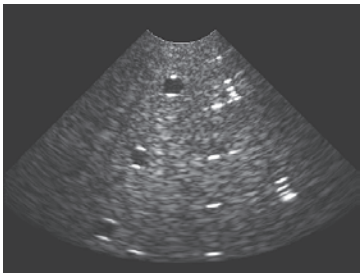

(d) The corrected image using the phase-aberration profiles derived using the steering angle-based sub-array method after manually adjusting ambiguity profiles.

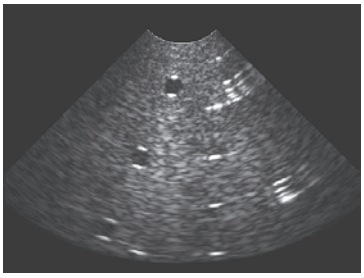

(e) The corrected image using the phase-aberration profiles derived using the image line-based sub-array method without adjusting ambiguity profiles

Fig. 15. Correction results using sub-arrays. (a) The corrected image using the measured phase-aberration profile at the 90° beam steering angle for all images lines. (b) The corrected image using the measured phase-aberration profile at the 105° beam steering angle for all images lines. (c) The corrected image using all 19 measured phase-aberration profiles (d) The corrected image using all 19 measured phase-aberration profiles with manually adjusted ambiguity profiles. (e) The corrected image using 19 measured phase-aberration profiles derived along image lines.

However, this process requires knowledge of the ambiguity profile for all directions, which is usually not available. A better way to measure the phase-aberration profile is to form common-midpoint beams along an image line (Li, 2000b), instead of at a steering angle. The advantage is that the focusing quality of each image pixel will not be influenced by the undetermined linear ambiguity profile; however, the image may still be distorted if the undetermined linear terms are very different for different image lines. The corrected image using this method is shown in Fig. 15(e). Compared with Fig. 15(c), the image quality for pixels near the transducer surface is improved in Fig. 15(e). Note that the derived aberration profiles are not adjusted for the undetermined different steering terms in this case.

4.2.2 Experimental results of correcting phase aberrations generated by incorrect pitch and speed values

The data set acquired from the phantom without the aberrator (Fig. 15(a)) was also used to demonstrate the capability of the sub-array method to correct phase aberrations generated by incorrect array pitch or propagation speed errors (Li et al., 2002). The synthetic aperture image formed using four incorrect pitch values and four incorrect speed values are shown in Figs. 16(a) and 17(a), respectively. The distortions are obvious.

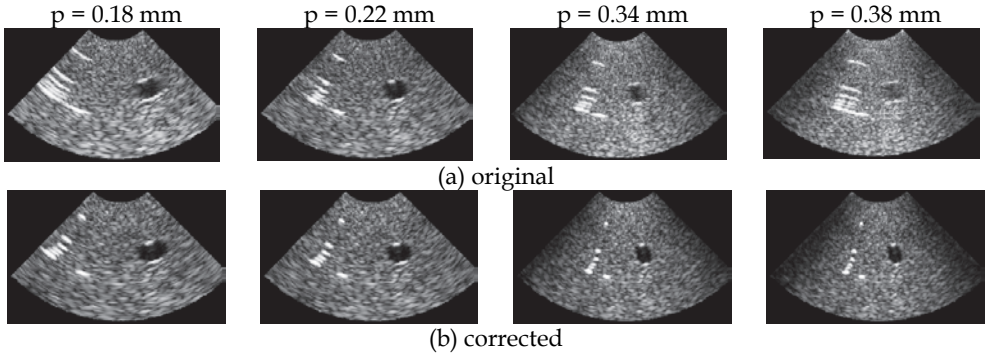

Fig. 16. Correction of phase aberrations generated by incorrect pitch values. (a) original images. (b) corrected images.

Phase aberration profiles were measured using the assumed pitch and speed values. The profile was again derived at 19 steering angles ($45^o \le \theta_i \le 135^o$ with 5^o interval) and signals around the nearest (to the transducer) point target, the cyst, and the farthest point target vertically below the nearest point target were used to derive three profiles for each direction, resulting in a total of 57 profiles. Figs. 16(b) and 17(b) show images after corrections. These results demonstrated that, after correction, the focusing quality in all the investigated cases is significantly improved in the whole image. These results also show distortions caused by the ambiguity profile (expansion and compression in both lateral and axial directions). The image is compressed (expanded) in the axial direction because the echo from a point target is treated as if it were from a target at a closer (farther) distance from the transducer when the speed is underestimated (overestimated). Different scales were used in Figs. 16 and 17 so that targets of interest occupy a similar image size as that in the un-aberrated image.

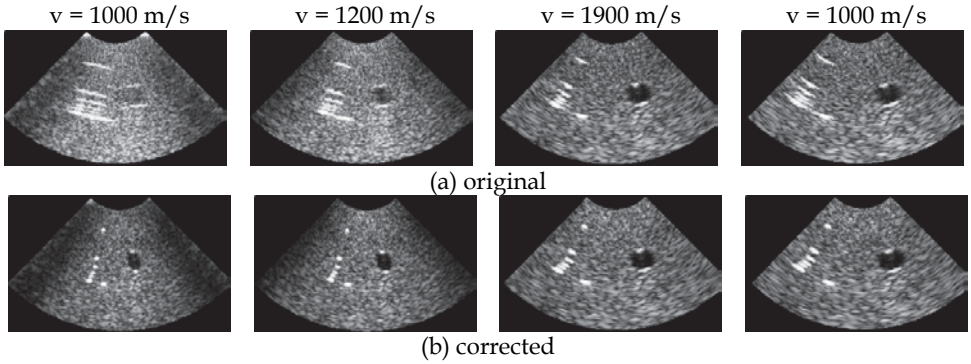

Fig. 17. Correction of phase aberrations generated by incorrect speed values. (a) original images. (b) corrected images.

4.2.3 Experimental results of system-error-difference calibration

The data set acquired using this phased-array system was also used to experimentally test the reciprocal signal algorithm for system-error-difference calibration (Li, 2008). The system has 48 transmission channels and 48 reception channels. Therefore each element has its own transmission and reception channels. Reciprocal signals acquired using each element (the reference element) in the transducer and all other elements were cross correlated. The cross-correlation coefficients between these reciprocal signals are shown in Fig. 18(a). All coefficients are very close to unity, except those that involve Element 12, which indicates that Element 12 was abnormal. Note that the cross-correlation coefficient between reciprocal signals acquired using the reference element and itself is also shown in Fig. 18(a), which is unity because the two reciprocal signals were the same signal. The peak positions of the cross-correlation functions are shown in Fig. 18(b) in grayscale. Each row in Fig. 18(b) is the derived system-error-difference profile using a different reference element. As a consequence, all rows should have identical shape but may have different offsets, if there was no noise (Li, 2008). This can be clearly seen in Fig. 18 (c), where the row profiles are plotted on top of one another. All the rows can be treated as the measurement result using a different element as the reference element. Its advantage is that only a small number of cross-correlation functions needs to be calculated. To improve the measurement accuracy, all row profiles can be averaged and it is shown in Fig. 18(d) together with the one standard deviation (each direction) lines. The profile should have a bias that is the average value of all system-error-difference values (Li, 2008). The peak-to-peak range of system-error-difference values of this system is less than 0.03 microseconds. The period of the transmitted signal at the center frequency (3.5 MHz) is about 0.29 microseconds. Therefore the difference between timing errors in the transmission and reception channels is less than one tenth of a period. Consequently, the transmission and reception phase-aberration profiles can be considered as the same for image formation. There is no need to separately measure transmission and reception channel-timing errors.

4.3 Algorithm for two-dimensional arrays

A few methods have been proposed to implement the near-field signal redundancy algorithm on a two-dimensional array. The all-row-plus-two-column algorithm (Li &

Robinson, 2000a) applies the one-dimensional near-field signal redundancy algorithm on all rows as well as the first and last columns of the transducer array, and then these results are combined to form a two-dimensional phase-aberration profile. However, the ambiguity profile of this method is not linear and a time-consuming iterative method has to be used to linearize the ambiguity profile. To solve this problem, an all-row-plus-two-column-and-a-diagonal algorithm has been proposed (Li & Robinson, 2007). In this algorithm, the one-dimensional algorithm is also applied to elements along a tilted line (the diagonal line if the array is square). The ambiguity profile of this algorithm is linear but it is very sensitive to noise. Another method, the cross algorithm (Li & Robinson, 2008), is based on the two-dimensional near-field signal-redundancy principle discussed in Section 3. In

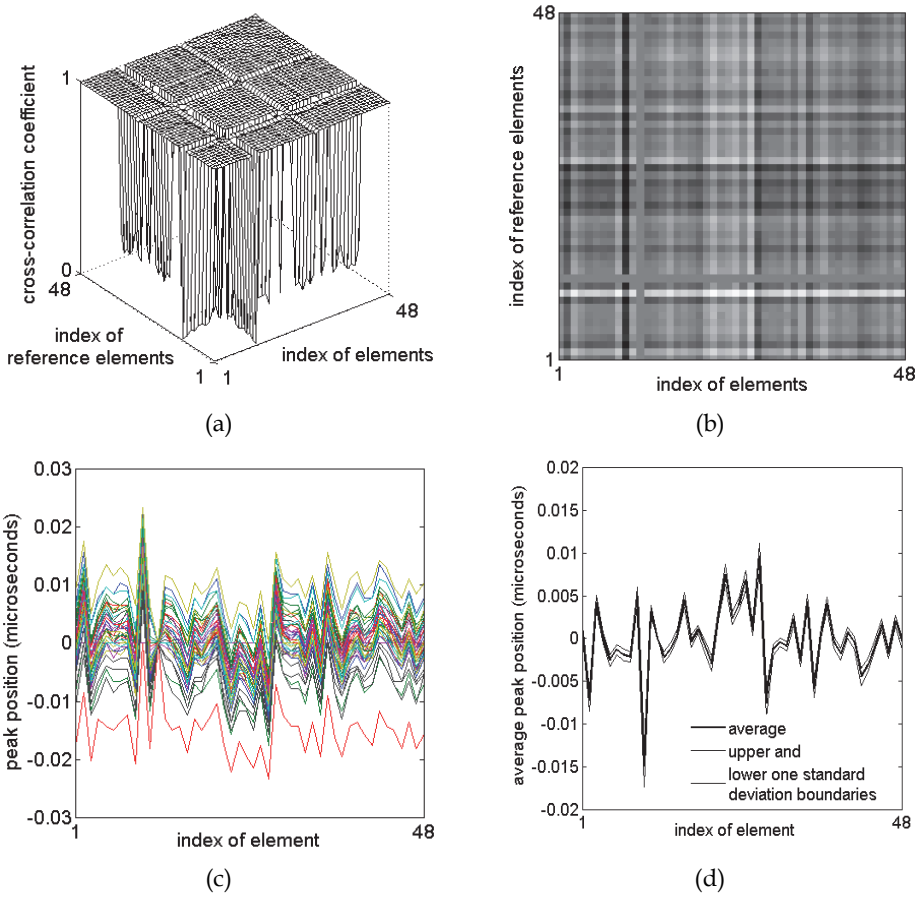

Fig. 18. (a) The cross-correlation coefficient distributions. (b) The peak positions distribution. (c) The peak positions profiles with all reference elements plotted on top of one another. (d) The derived system-error-difference profile by averaging profiles derived with all reference elements. The boundaries of one standard deviation are also plotted.

this algorithm, most common-midpoint signals are acquired using four adjacent transducer elements, which is not available in one-dimensional arrays. An initial two dimensional phase-aberration profile is derived from the peak positions of cross-correlation functions between these common midpoint signals. The boundary conditions needed to drive the final phase-aberration profile are derived by applying the one-dimensional-array algorithm to the first row and the first column of the array. The cross algorithm has a linear ambiguity profile and high signal-to-noise ratio. Due to the lack of experimental data from two-dimensional arrays (still hard to build), the discussed algorithms for two-dimensional arrays have only been tested using simulated data (Li, & Robinson, 2000a, 2007, 2008).

5. Conclusion

Compared with astromical imaging, phase-aberration correction in medical ultrasound imaging is more challenging in the sense that targets are in the near field and aberrators can exist anywhere between the interested targets and the array. Many successful algorithms used in astromical imaging are based on the signal-redundancy principle. However, this principle is invalid in the near field. To use the signal redundancy principle for phase-aberration correction in medical ultrasound images, the near-field effects have to be managed. In this chapter, the near-field signal-redundancy principle has been discussed in depth. Common-midpoint signals are still a special group of signals in the near field because they can be considered as redundant after a dynamic near-field-delay correction. Based on the near-field signal-redundancy principle, phase-aberration-correction algorithms have been developed for linear arrays, phased arrays, and two-dimensional arrays. There are three basic requirements for these algorithms to work properly. One of the requirements is that the phase-aberration effects of aberrators between targets in a region of interest and the transducer array can be approximately modelled as the effects of a phase screen on the transducer surface. The second requirement is that the element size is small enough so that the phase aberration value of the phase screen under each element can be considered as the same. The third requirement is that multi-path echoes are ignorable in common-midpoint signals, because they are not redundant.
The linear array algorithm has been successfully tested on transverse scan of abdomen of volunteers. At this body position, the aberrators are mainly muscle and fat layers under the skin (close to the transducer surface), which makes it easier to model their effect as that of a phase screen on the transducer surface. Another property of the body structure at this location and the transducer orientation is that the thickness of the fat and muscle layers changes very slowly in the direction of element height (10 mm). This property makes it easier to satisfy the second requirement. The high cross-correlation coefficient between common-midpoint signals (Li et al., 1997) also indicated that multi-path echoes were weak in common-midpoint signals and the third requirement was satisfied. Experimental results also show that the measured phase aberration profiles were different for targets from different depths. This could be because the aberration effect of fat and muscle layers near the transducer surface is different for targets at different depths, which is similar to the effect of the aberrator attached to the phased-array transducer surface in phased-array experiments (Section 4.2.1), where the phase screen was different for echoes from targets in different directions. Another possible reason is that the effect of other aberrators between the targets and the transducer surface was included.
For other imaging positions on the body, small element size in both dimensions is usually required to sample the phase screen properly (the second requirement). That is, a two-

dimensional array is needed, but it is still difficult and expensive to build a two-dimensional array. When two-dimensional arrays become available, the near-field signal redundancy algorithm should work at more imaging positions. However, there will be imaging positions where the structure is so complex that the three basic requirements are not satisfied. In this case, the cross-correlation coefficient between common midpoint signals will be low and it can be used as the trigger to abandon the correction.

6. Acknowledgment

The author would like to thank Brent Robinson for many helpful discussions and providing many experimental and simulated data sets.

7. References

Buffington, A.; Crawford, F. S.; Muller, R. A.; Schwemin, A. J. & Smits, R. G. (1997). Correction of atmospheric distortion with an image-sharpening telescope. *J. Opt. Soc. Am.*, Vol. 67, No. 3, (March 1977), pp. 298-303, ISSN: 1084-7529

Goodman, J. W.; Huntley, W. H.; Jackson, Jr., D. W. & Lehmann, M. (1966). Wavefront-reconstruction imaging through random media. *Appl. Phys. Lett.,* Vol. 8, No. 12, (June 1966), pp. 311-312, ISSN: 0003-6951

Hamaker, J. P.; O'Sullivan, J. D. & Noordam, J. E. (1977). Image sharpness, Fourier optics, an redundant-spacing interferometry. *J. Opt. Soc. Am.,* Vol. 67, No. 9, (August 1977), pp. 1122-1123, ISSN: 1084-7529

Hinkelman, L. M.; Mast, T. D., Metlay, L. A., and Waag, R. C. (1998). The effect of abdominal morphology on ultrasonic pulse distortion. Part I. Measurements. *J. Acoust. Soc. Am.* Vol. 104, No. 6, pp. 3635-3649, ISSN: 0001-4966, December 1998.

Hirama M. & Sato, T. (1984). Imaging through an inhomogeneous layer by least-mean-square error fitting. *J. Acoust. Soc. Am*. Vol. 75, No. 4, (April 1984), pp. 1142-1147, ISSN: 0001-4966

Hogg, D. C.; Guirand, F. O & Deckere, M. T. (1981). Measurement of excess radio transmission length on earth-space paths. *Astron. Astrophys.*, Vol. 95, No. 2, (March 1981), pp. 304-307, ISSN: 0004-6361

Ishiguro, M. (1974). Phase error correction in multi-element radio interferometer by data processing. *Astron. Astrophys. Suppl. Ser.*, Vol. 15, (June 1974), pp. 431-443, ISSN: 0004-6361

Jennison, R. C. (1958). A phase sensitive interferometer technique for the measurement of the Fourier transforms of spatial brightness distributions of small angular extent. *Mon. Not. R. Astron. Soc.*, Vol. 118, No. 3, (January 1958), pp. 276-284, ISSN: 1365-2966

Li, Y. & Robinson, B. (2008). The Cross algorithm for phase-aberration correction in medical ultrasound images formed with two-dimensional arrays. *IEEE Trans. Ultrason., Ferroelect., Freq. Cont.*, Vol.55, No.3, (March 2008), pp. 588-601, ISSN 0885-3010

Li, Y. (2008). Timing-error-difference calibration using reciprocal signals. *IEEE Trans. Ultrason., Ferroelect., Freq. Cont.*, Vol.55, No.11, (November 2008), pp. 2405-2417, ISSN 0885-3010

Li, Y. & Robinson, B. (2007). Implementation of the near-field signal redundancy phase-aberration correction algorithm on two-dimensional arrays. *IEEE Trans. Ultrason., Ferroelect., Freq. Cont.*, Vol.54, No.1, (January 2007), pp. 42-51, ISSN 0885-3010

Li, Y. (2002a). The influences of ambiguity phase aberration profiles on focusing quality in the very near field -- part I: single range focusing on transmission. *IEEE Trans. Ultrason., Ferroelect., Freq. Cont.*, Vol.49, No.1, (January 2002), pp. 57-71, ISSN 0885-3010

Li, Y. (2002b). The influences of ambiguity phase aberration profiles on focusing quality in the very near field -- part II: dynamic range focusing on reception. *IEEE Trans. Ultrason., Ferroelect., Freq. Cont.*, Vol.49, No.1, (January 2002), pp. 72-84, ISSN 0885-3010

Li, Y.; Robinson, B.; Drew, P.; Wilson, L.; Price, D. & Gill, R. (2002). Correction of distributed phase aberrations caused by propagation-speed and array-pitch errors. *Proceedings of 2002 IEEE International Ultrasonics Symposium*, pp. 1687-1691, ISBN 0-7803-7583-1, Munich, Germany, October 2002

Li, Y. & Robinson, B (2000a). Phase aberration correction using near-field signal redundancy: two-dimensional array algorithm. *Proceedings of 2000 IEEE International Ultrasonics Symposium*, pp. 1729-1733, ISBN 0-7803-6365-5, *San Juan, Puerto Rico*, October 2000.

Li, Y. & Robinson, B. (2000b). Small-element-array algorithm for correcting phase aberration using near-field signal redundancy-- part II: experimental results. *IEEE Trans. Ultrason., Ferroelect., Freq. Cont.*, Vol.47, No.1, (January 2000), pp. 49-57, ISSN 0885-3010

Li, Y. (2000a). Phase and/or amplitude aberration correction for imaging--continuation. *US Patent Number*: 6,120,450. September 19, 2000

Li, Y. (2000b). Small-element-array algorithm for correcting phase aberration using near-field signal redundancy--part I: principles. *IEEE Trans. Ultrason., Ferroelect., Freq. Cont.*, Vol.47, No.1, (January 2000), pp. 29-48, ISSN 0885-3010

Li, Y. & Gill, R. (1998). A comparison of matched signals used in three different phase-aberration correction algorithms. *Proceedings of 1998 IEEE International Ultrasonics Symposium*, pp. 1707-1712, ISBN 0-7803-4095-7, Sendai, Miyagi, Japan, October 1998.

Li, Y. (1997). Phase-aberration correction using near-field signal redundancy--part I: Principles. *IEEE Trans. Ultrason., Ferroelect., Freq. Cont.*, Vol.44, No.2, (March 1997), pp. 355-371, ISSN 0885-3010

Li, Y.; Robinson, D. & Carpenter D. (1997). Phase-aberration correction using near-field signal redundancy--part II: experimental results. *IEEE Trans. Ultrason., Ferroelect., Freq. Cont.*, Vol.44, No.2, (March 1997), pp. 372-379, ISSN 0885-3010

Li, Y. & Robinson, B. (1997). Phase-aberration-correction algorithm for phased-array transducers using near-field signal redundancy. *Proceedings of 1997 IEEE International Ultrasonics Symposium*, pp. 1729-1732, ISBN 0-7803-4153-8, Ontario, Canada, October 1997.

Li, Y.; Robinson, D.; Carpenter, D. & Kossoff, G. (1996). Phase-aberration correction using near-field signal redundancy: correcting phase aberrations caused by medium-velocity and array-pitch Errors. *Proceedings of 1996 IEEE International Ultrasonics Symposium*, pp. 1367-1370, ISBN 0-7803-3615-1, San Antonio, Texas, November 1996.

Muller, R. A. & Buffington, A. (1974). Real-time correction of atmospherically degraded telescope images through image sharpening. *J. Opt. Soc. Am.*, Vol. 64, No. 9, (September 1974), pp. 1200-1209, ISSN: 1084-7529

O'Donnell M. & Flax, S. W. (1988). Phase aberration measurements in medical ultrasound: human study. *Ultrasonic Imaging*, Vol. 10, No. 1, (January 1988), pp. 1-11, ISSN 0161-7346

Rachlin, D. (1990). Direct estimation of aberration delays in pulse-echo image systems. *J. Acoust. Soc. Am*. Vol. 88, No. 1, (July 1990),pp. 191-198, ISSN: 0001-4966

Robinson, B. S.; Shmulewitz, A. & Burke, T. M. (1994). Waveform aberrations in an animal model. *1994 IEEE Ultrasonics Symposium,* pp. 1619-1624, ISBN: 0-7803-2012-3, Cannes France, November 1994

Shmulewitz, A.; Teefey, S. A. & Robinson, B. S. (1993). Factors affecting image quality and diagnostic efficacy in abdominal sonography: a prospective study of 140 patients," *J. Clinical Ultrasound*, Vol. 21, No. 9, (November 1993), pp. 623-630, ISSN: 1097-0096

Steinberg B. D. & Subbaram, H. M. (1991). Microwave imaging technique. Wiley, ISBN: 047150078X , New York, USA

Tyson, R. K. (2010). *Principle of adaptive optics*. CRC Press, ISBN: 978-1-4398-0859-7, Bota Recon, USA

Yilmaz, O. & Doherty, S. M. (1987). Seismic data processing. *Society of Exploration Geophysicists*, ISBN 10: 0931830400, Tulsa, USA

Zhu, Q. & Steinberg, B. D. (1992). Large transducer measurements of wavefront distortion in the female breast. *Ultrasonic Imaging*, Vol. 14, No. 3, (July 1992), pp. 276-299, 1992. , ISSN 0161-7346

Ultrasound Imaging - Medical Applications

Edited by Prof. Oleg Minin

ISBN 978-953-307-279-1
Hard cover, 330 pages
Publisher InTech
Published online 23, August, 2011
Published in print edition August, 2011

This book provides an overview of ultrafast ultrasound imaging, 3D high-quality ultrasonic imaging, correction of phase aberrations in medical ultrasound images, etc. Several interesting medical and clinical applications areas are also discussed in the book, like the use of three dimensional ultrasound imaging in evaluation of Ashermanâ€™s syndrome, the role of 3D ultrasound in assessment of endometrial receptivity and follicular vascularity to predict the quality oocyte, ultrasound imaging in vascular diseases and the fetal palate, clinical application of ultrasound molecular imaging, Doppler abdominal ultrasound in small animals and so on.

INTECH
open science | open minds

InTech Europe
University Campus STeP Ri
Slavka Krautzeka 83/A
51000 Rijeka, Croatia
Phone: +385 (51) 770 447
Fax: +385 (51) 686 166
www.intechopen.com

InTech China
Unit 405, Office Block, Hotel Equatorial Shanghai
No.65, Yan An Road (West), Shanghai, 200040, China
中国上海市延安西路65号上海国际贵都大饭店办公楼405单元
Phone: +86-21-62489820
Fax: +86-21-62489821